

Supplement of Ocean Sci., 16, 1183–1205, 2020
<https://doi.org/10.5194/os-16-1183-2020-supplement>
© Author(s) 2020. This work is distributed under
the Creative Commons Attribution 4.0 License.



Supplement of

An explicit estimate of the atmospheric nutrient impact on global oceanic productivity

Stelios Myriokefalitakis et al.

Correspondence to: Stelios Myriokefalitakis (steliosm@noa.gr) and Matthias Gröger (matthias.groeger@io-warnemuende.de)

The copyright of individual parts of the supplement might differ from the CC BY 4.0 License.

Supplementary Tables

Table S1: Physical forcing fields provided at a daily time step.

Field	Units
Water flux into seawater	kg/m ² /s
Mixed layer depth	m
Surface net downward shortwave flux	W/m ²
Wind speed	m/s
Ice concentration	%
Water flux due to freezing/melting	kg/m ² /s
Tracer diffusive fluxes along the bottom boundary layer	m ³ /s
River runoff	kg/m ² /s
Ocean vertical salt diffusivity	m ² /s
Horizontal divergence transport	1/s
Seawater salinity	g/kg
Seawater potential temperature	°C
Effective ocean transports	m ³ /s

Supplementary Figures

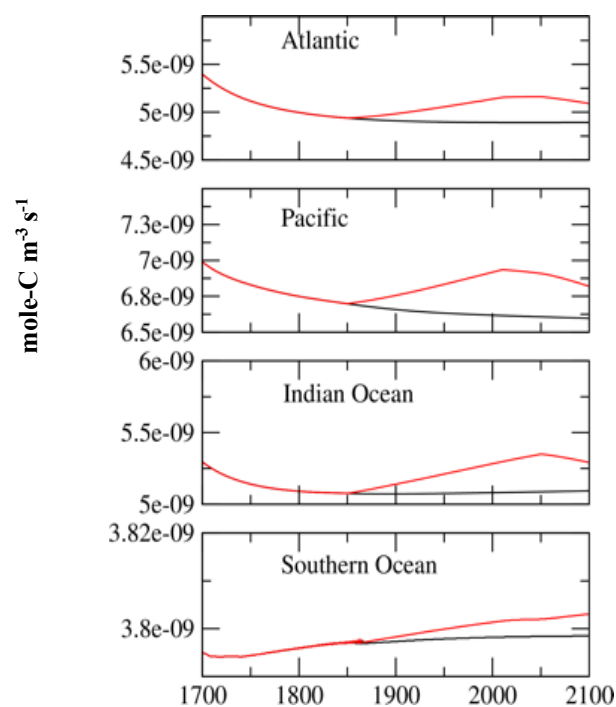


Figure S1: Area averaged annual mean primary production in mole C m⁻³ s⁻¹ for the main ocean basins (Atlantic, Pacific, Indian and Southern Oceans). Red lines indicate primary production rates for the STD simulation and black lines for the CTRL simulation, respectively.

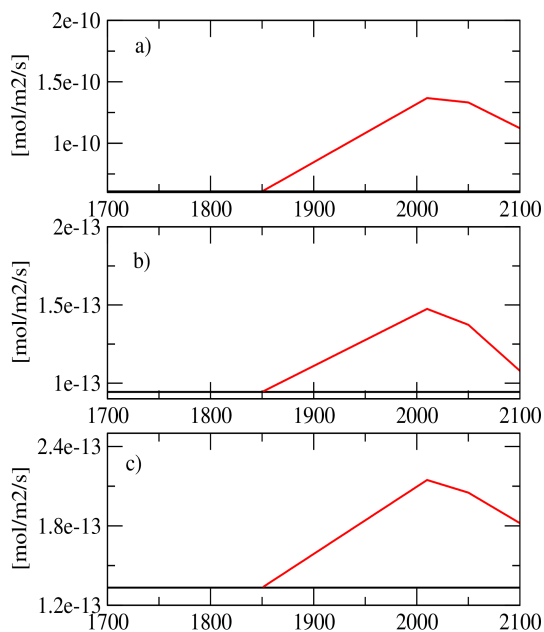


Figure S2: Globally averaged atmospheric deposition fluxes (red lines) of a) nitrogen, b) phosphorous, and c) iron in mol m⁻² s⁻¹, as taken into account in PISCES. The black line indicates forcing for the control run under preindustrial conditions (i.e., year 1850).

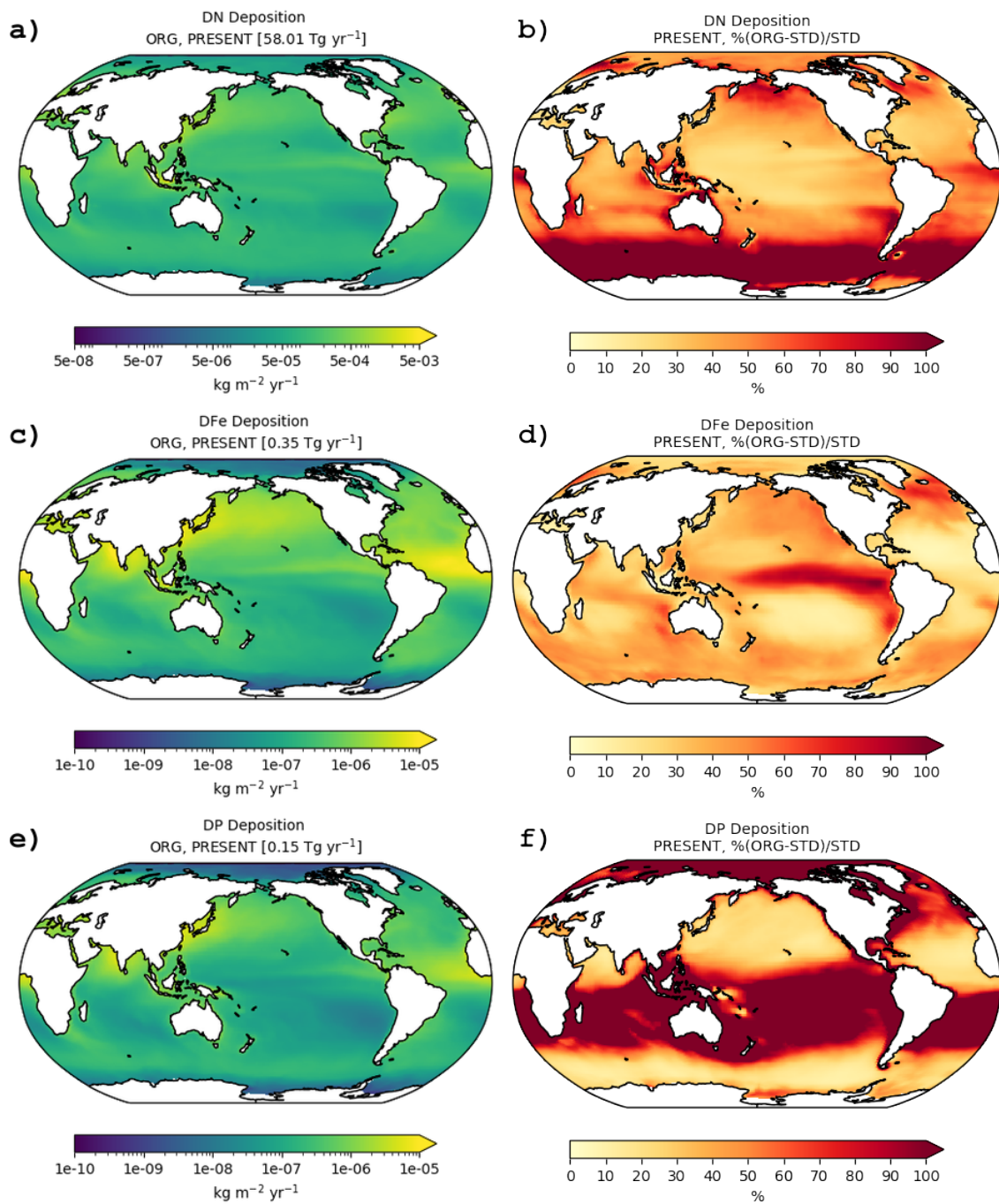


Figure S3: Atmospheric deposition fluxes (left column) into the ocean of dissolved nitrogen (a), iron (c), and phosphorus (e) considered by the model for the ORG simulation for PRESENT (2001–2020 average), and the respective percentage differences (b,d,f) compared to the STD simulation (right column).

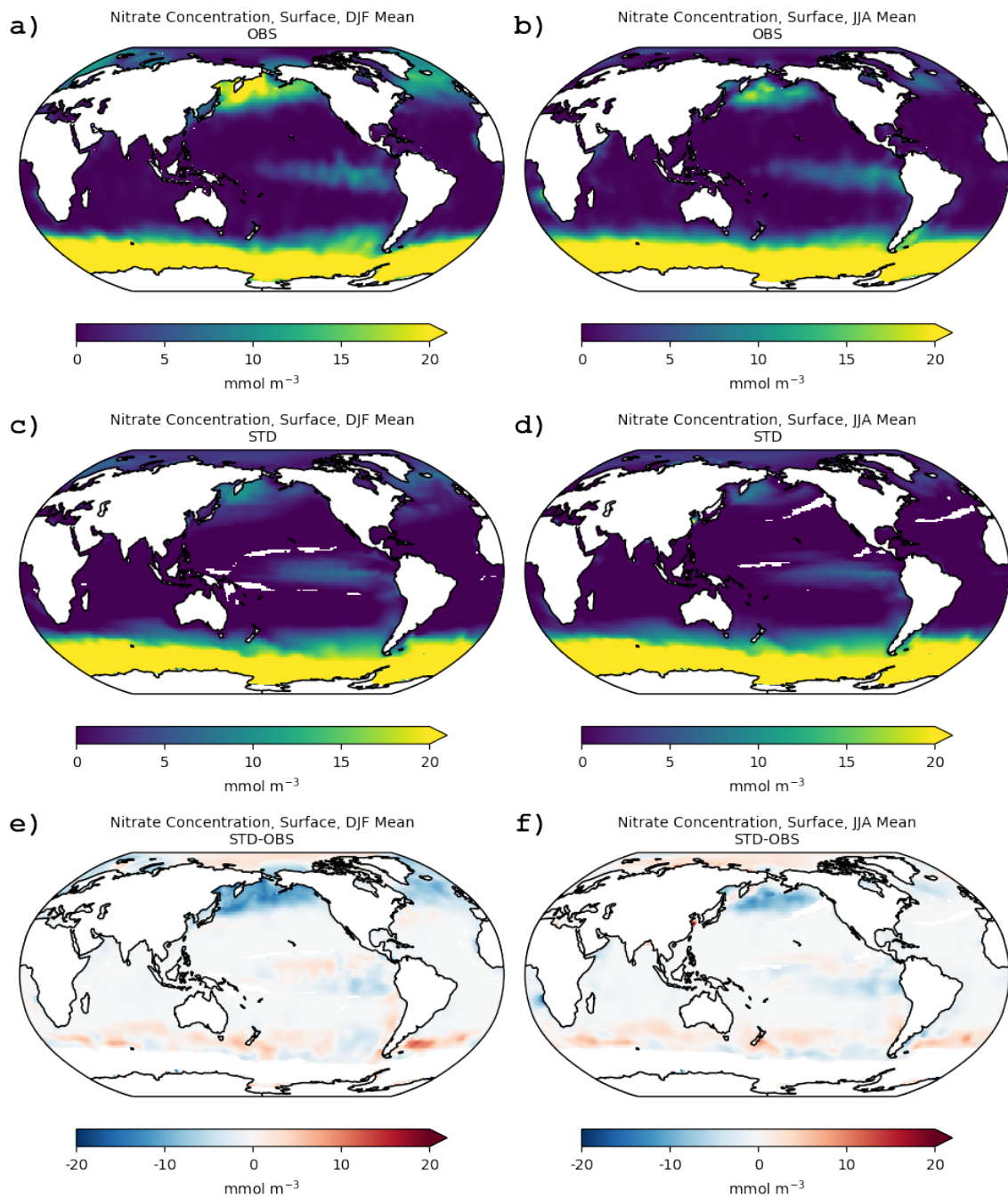


Figure S4: Surface nitrate concentrations (mmole m^{-3}) for the boreal winter (DJF; left column) and summer (JJA; right column) seasons as compiled from the World Ocean Atlas (WOA; Garcia et al., 2010b) (a,b), the simulated concentrations for PRESENT as simulated for STD (c,d), and the absolute differences compared to observations (e,f); observational and modeled data have been averaged over a $1^\circ \times 1^\circ$ horizontal resolution.

5

Figure S4 illustrates the comparison between the simulated present-day surface nitrate concentration and the compiled data from the World Ocean Atlas (WOA; Garcia et al., 2010b) for two seasons: the boreal winter (December, January, and February; DJF) and the boreal summer (June, July, and August; JJA). Generally, the model compares quite well with the nitrate surface observations. However, compared to the WOA compilation (Figs. S4a,b) the modeled nitrate concentrations (Figs. S4c,d, respectively) are lower in the northern high latitudes for both seasons ($\sim 5\text{-}10 \text{ mmol/m}^3$), especially in the Subpolar Pacific Ocean (up to 30 mmol/m^3) during DJF. This is likely related to the model's too shallow mixed layer thickness (not shown) and, as a consequence, the transport of nutrients and from deeper layers to the surface is likewise underestimated during the winter season. On the other hand, the surface nitrate concentrations are somewhat overestimated in the Southern Ocean for both seasons (Figs. S4e,f). This is also the case when the model uses PISCES default atmospheric deposition fields and it might be related to deficiencies in the model's abiotic processes. As also explained by Aumont et al. (2015), the WOA climatology may be, however, biased toward lower values since most of the observational data have been collected during the productive season in that region.

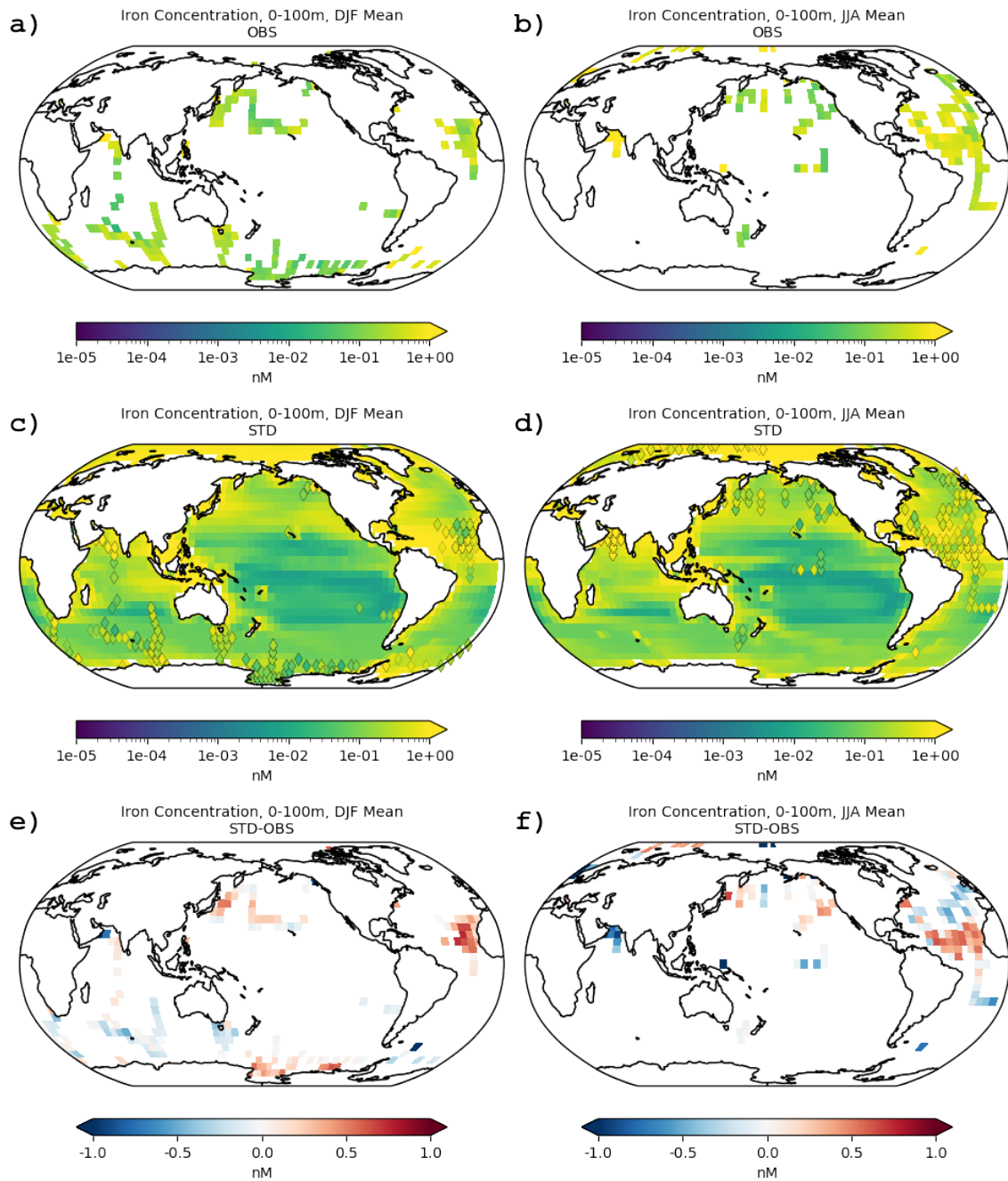


Figure S5: Iron concentrations (nM) averaged in the upper 100m for the boreal winter (DJF; left column) and summer (JJA; right column) seasons (a,b) as compiled by Tagliabue et al. (2012) (OBS), the respective simulated concentrations for PRESENT (c,d) as simulated for STD (diamond symbols represent observation data), and the respective absolute differences (e,f); observational and modeled data have been averaged over a $5^\circ \times 5^\circ$ horizontal resolution.

5

Figure S5 presents a comparison of the modeled with observed oceanic iron concentrations in the upper 100m, for two seasons (DJF and JJA). The DFe oceanic observation data (Figs. S5a,b) are taken from Tagliabue et al. (2012) (<https://www.bodc.ac.uk/geotraces/data/historical/>; last access 29/02/2020). The model simulates reasonably the observed oceanic iron concentrations for both seasons, for the STD simulation (Figs. S5c,d). The observed low oceanic DFe concentrations are well captured in most of the cases by the model, especially for boreal winter (Fig. S5d), but underestimated during boreal summer (Fig. S5d). Low dissolved iron concentrations of about 0.1 nM (i.e., 1nM = 10⁻⁹ moles per liter) are simulated and observed in the subtropical Atlantic and Pacific basins, especially in the HNLC regions. The high observed oceanic DFe concentrations (>1 nM) are also well simulated along the coasts and over the continental margins, as a result of sediment mobilization. In the vicinity of intense dust sources, such as the Sahara, the upper ocean in the model is strongly influenced by the atmospheric inputs, and some higher values compared to observations (up to 0.5 nM) are simulated in the North Atlantic Ocean, for both seasons. The model also slightly overestimates the observed DFe concentrations in the North Pacific, as well as in the subpolar Southern Ocean (Pacific sector) during the local summer season. This may be related to the too low consumption of nutrients, as the model may underestimate the biological production in this area (see Sect. 3). In the subtropical South Atlantic, the low DFe oceanic concentrations are well captured, although during boreal summer the model slightly underestimates the observations. In the Southern tropical Pacific during boreal summer, the low surface concentrations for the Fe-limited latitudes are also underestimated. Moreover, across the Southern Ocean (except for the subpolar sector) the model calculates lower values for the DFe concentrations.

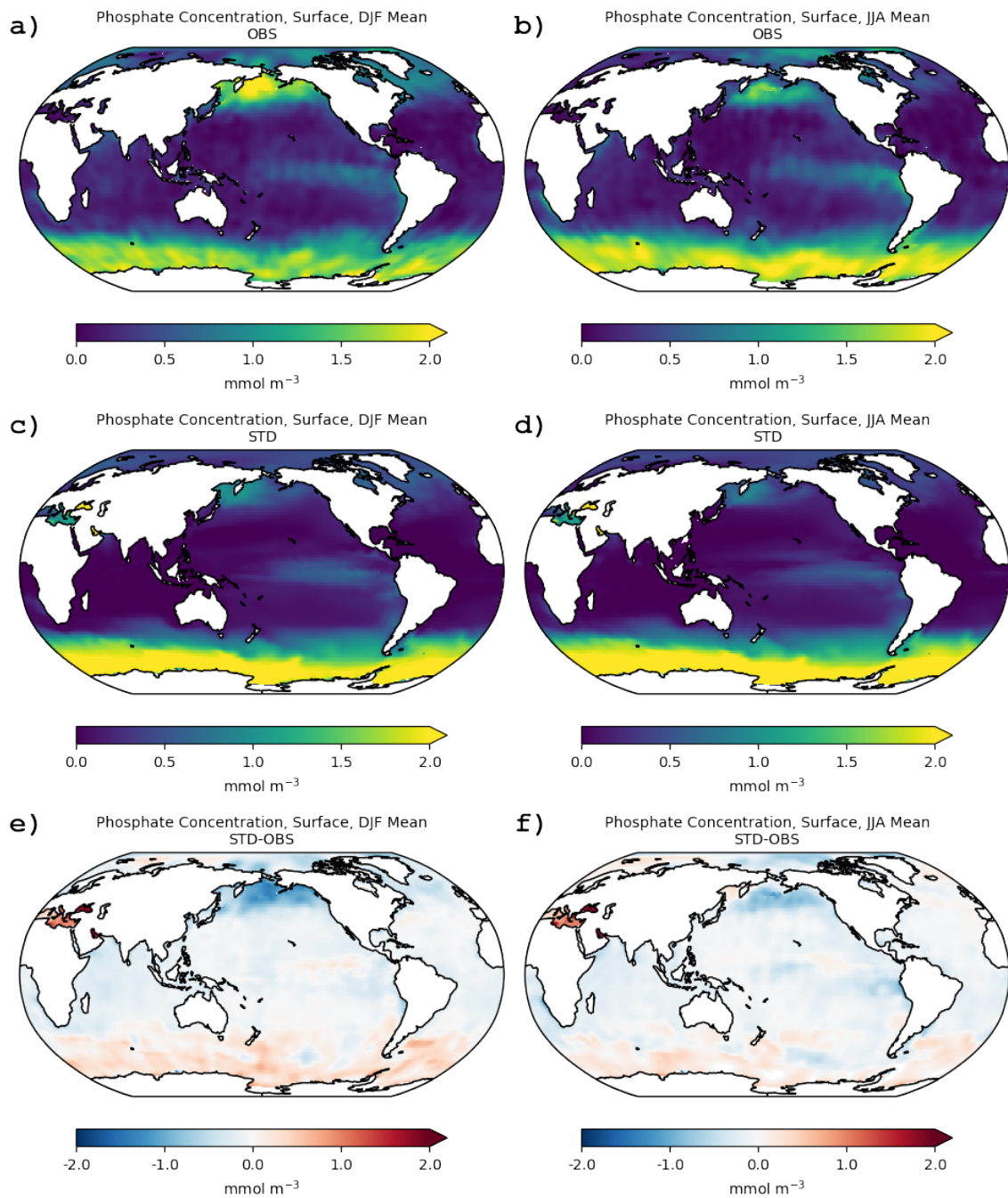


Figure S6: Surface phosphate concentrations (mmole m^{-3}) for the boreal winter (DJF; left column) and summer (JJA; right column) seasons as compiled from the World Ocean Atlas (WOA; Garcia et al., 2010b) (a,b), the simulated present-day surface concentrations for PRESENT as simulated for STD (c,d), and the respective absolute differences (e,f); observational and modeled data have been averaged over a $1^\circ \times 1^\circ$ horizontal resolution.

Figure S6 compares the simulated surface phosphate concentration with an observation-based data set from WOA, for the summer and winter seasons. The global pattern of observed phosphate is mainly controlled by the ocean dynamics and it is well reproduced by the model. Hence, during winter enhanced wind mixing and convective mixing transport nutrient-rich deep water to the surface in the North Atlantic and North Pacific. At the same time, nutrient consumption by biological productivity in the high latitudes is weak due to low winter temperatures and reduced light conditions. The resulting maximum phosphate concentrations in the Atlantic and Pacific subpolar gyres, however, are somewhat underestimated (up to 1.5 mmol m^{-3}) by the model compared to the WOA data (Figs. S6a,b). This is also caused by a too shallow winter mixed layer depth simulated by the physical model NEMO as forced by the OMIP standard forcing.

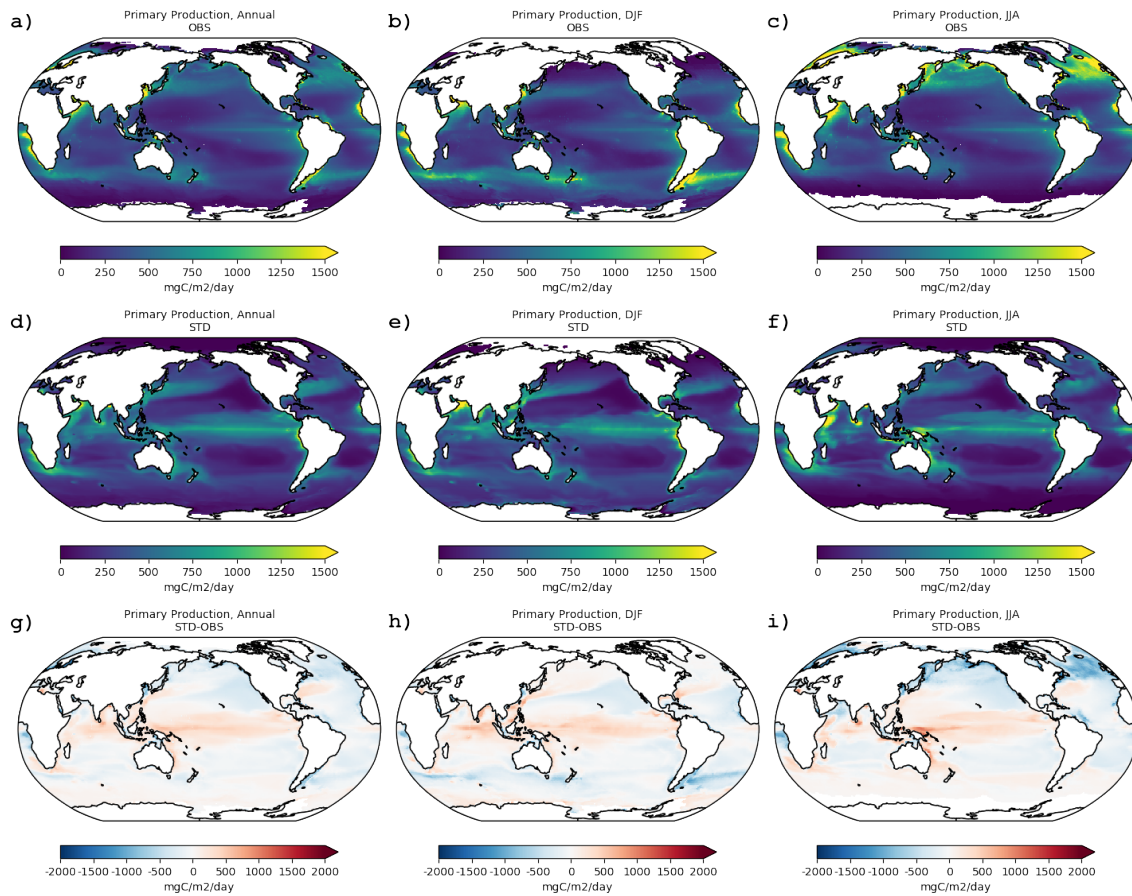


Figure S7: Primary production ($\text{mg-C m}^{-2} \text{ day}^{-1}$) for annual (left column), boreal winter (DJF; middle column), and summer (JJA; right column) seasons, as derived based on satellite-based estimates from SeaWiFS (Behrenfeld et al., 2005) (a,b,c), the simulated integrated primary production for the STD simulation for PRESENT (d,e,f), and the respective absolute differences (g,h,i); satellite-based and modeled data have been averaged over a $1^\circ \times 1^\circ$ horizontal resolution.

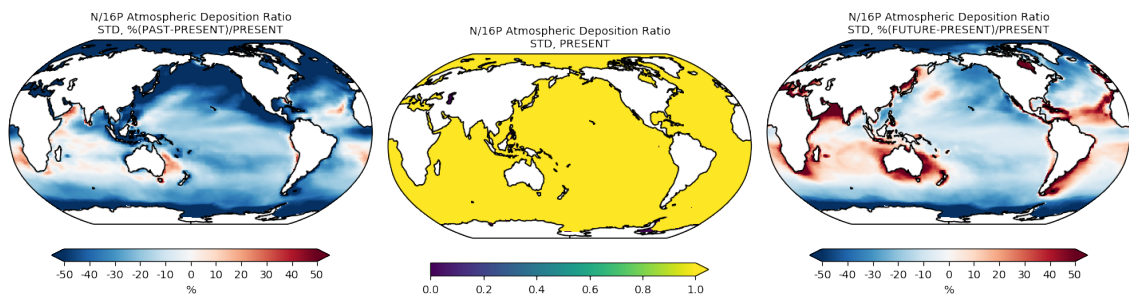
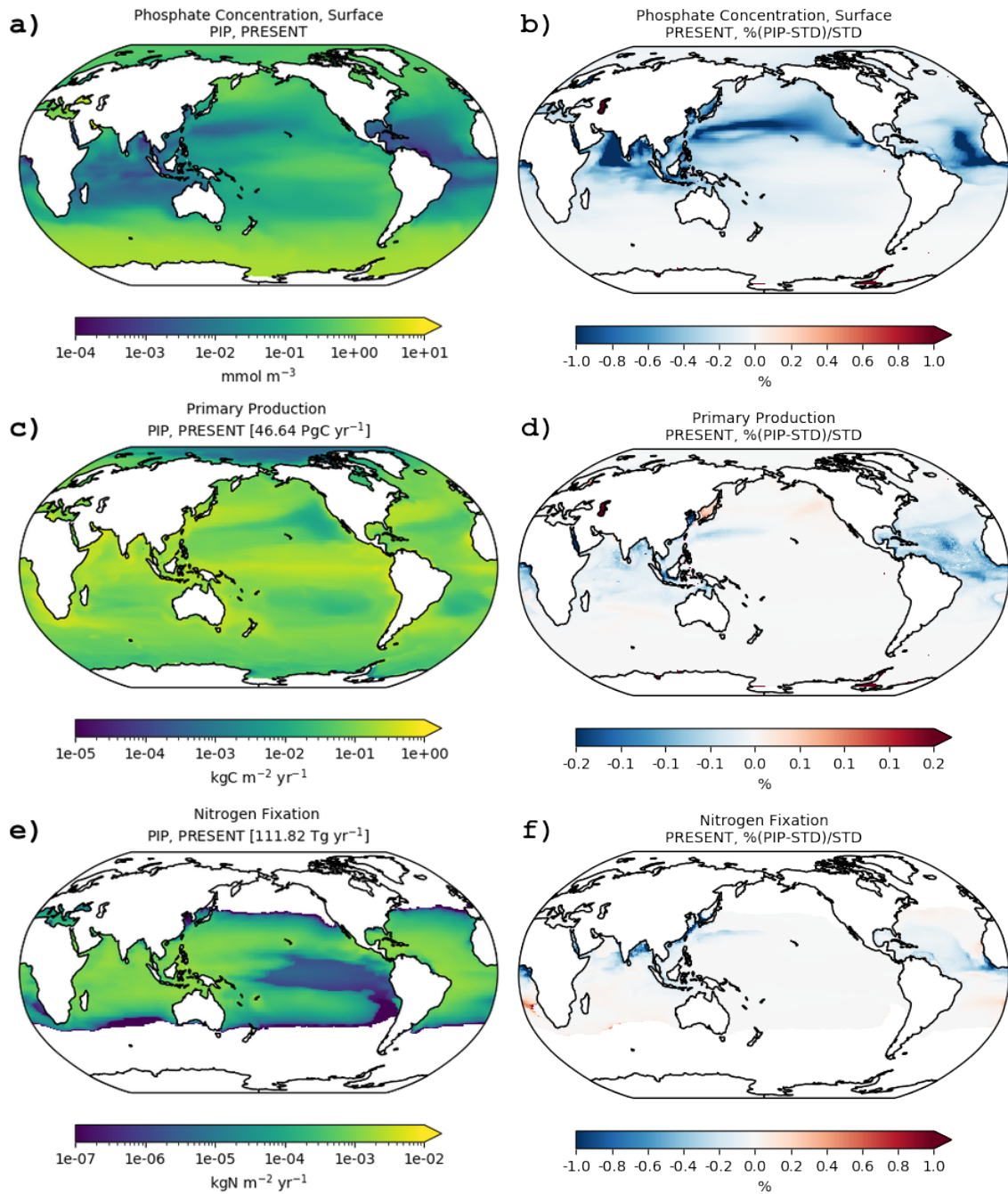


Figure S8: Atmospheric nutrient deposition fluxes relative to the Redfield ratio for PRESENT (middle) and the relative changes for PAST (left) and FUTURE (right) for the STD simulation; values >1.0 denotes excess of nitrogen compared to phosphorus.

5



5 **Figure S9: Surface oceanic concentrations (mmol m^{-3}) of phosphate (top row), primary production rates ($\text{kg-C m}^{-2} \text{yr}^{-1}$) (middle row), and nitrogen fixation ($\text{kg-N m}^{-2} \text{yr}^{-1}$) (bottom row), as calculated by the model for PRESENT for the sensitivity PIP simulation (i.e., as for STD, but keeping phosphorus atmospheric deposition to preindustrial levels) (left column), and the respective relative differences (%) to the STD simulation (right column).**

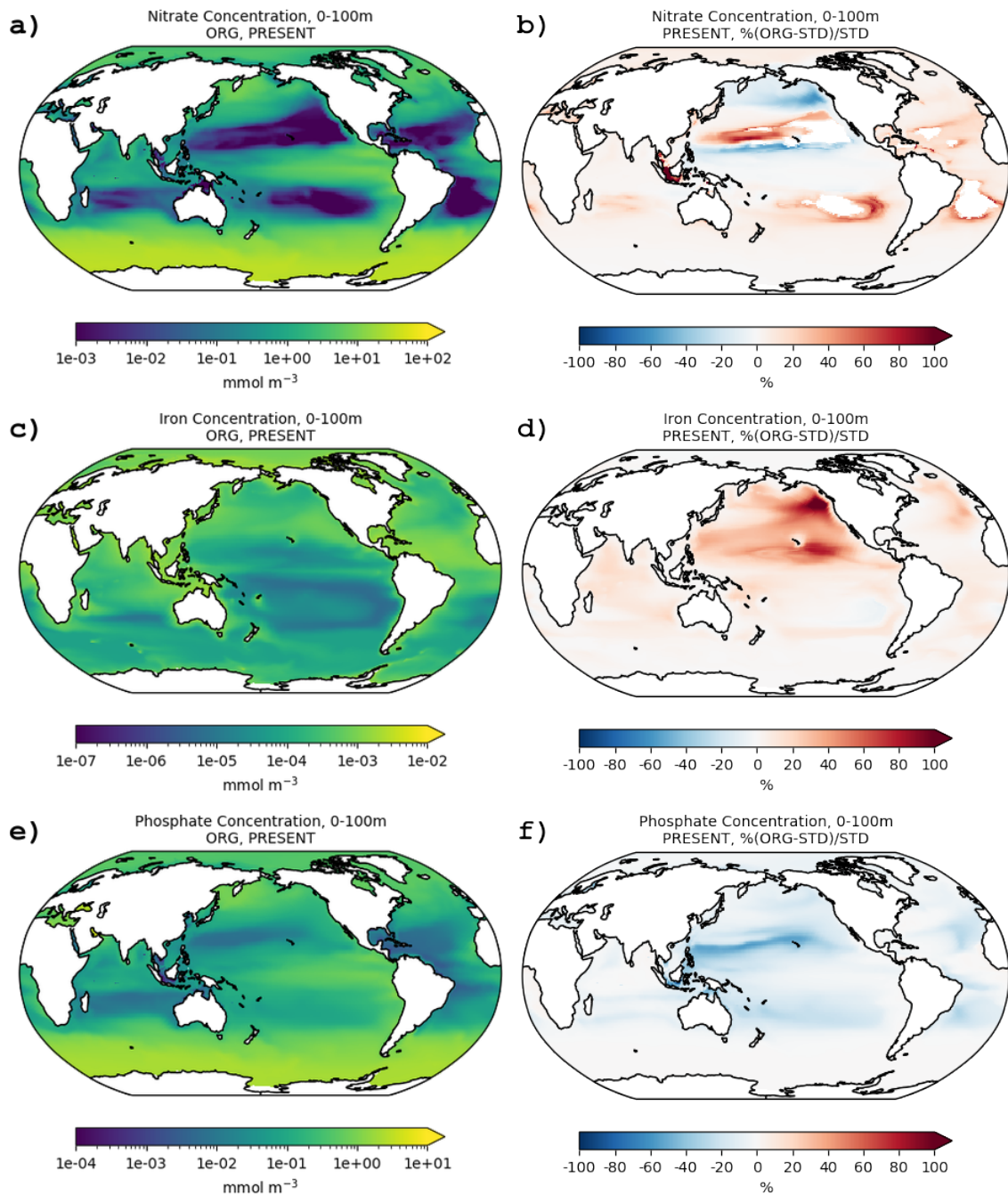


Figure S10: Oceanic concentrations averaged over the upper 100m (left column) of nitrate (a), iron (c) and phosphate (e) as calculated by the model for the ORG simulation for PRESENT (2001–2020 average), and the respective percentage differences (b,d,f) compared to the STD simulation (right column).

5

References

- Aumont, O., Ethé, C., Tagliabue, A., Bopp, L. and Gehlen, M.: PISCES-v2: an ocean biogeochemical model for carbon and ecosystem studies, *Geosci. Model Dev.*, 8(8), 2465–2513, doi:10.5194/gmd-8-2465-2015, 2015.
- Behrenfeld, M. J., Boss, E., Siegel, D. A. and Shea, D. M.: Carbon-based ocean productivity and phytoplankton physiology
5 from space, *Global Biogeochem. Cycles*, 19(1), 1–14, doi:10.1029/2004GB002299, 2005.
- Garcia, H. E., Locarnini, R. A., Boyer, T. P., Antonov, J. I., Zweng, M. M., Baranova, O. K. and Johnson, D. R.: WORLD OCEAN ATLAS 2009 Volume 4: Nutrients (phosphate, nitrate and silicate), U.S. Government Printing Office, Washington, D.C., 2010.
- Tagliabue, A., Mtshali, T., Aumont, O., Bowie, A. R., Klunder, M. B., Roychoudhury, A. N. and Swart, S.: A global
10 compilation of dissolved iron measurements: focus on distributions and processes in the Southern Ocean, *Biogeosciences*, 9(6), 2333–2349, doi:10.5194/bg-9-2333-2012, 2012.